Automated search for optimal surface phases (ASOPs) in grand canonical ensemble powered by machine learning

Dongxiao Chen, 🆔 Cheng Shang and 🆔 Zhi-Pan Liu

COLLECTIONS

Paper published as part of the special topic on Chemical Design by Artificial Intelligence

View Online   Export Citation   CrossMark

ARTICLES YOU MAY BE INTERESTED IN

Coupled cluster downfolding methods: The effect of double commutator terms on the accuracy of ground-state energies
The Journal of Chemical Physics **156**, 094106 (2022); https://doi.org/10.1063/5.0076260

$\Delta \mathrm{NO}$ and the complexities of electron correlation in simple hydrogen clusters
The Journal of Chemical Physics **156**, 094102 (2022); https://doi.org/10.1063/5.0073227

Real-space density kernel method for Kohn–Sham density functional theory calculations at high temperature
The Journal of Chemical Physics **156**, 094105 (2022); https://doi.org/10.1063/5.0082523
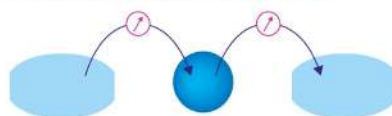
Automated search for optimal surface phases (ASOPs) in grand canonical ensemble powered by machine learning

View Online   Export Citation   CrossMark

Dongxiao Chen,[1] Cheng Shang,[1,2] (iD) and Zhi-Pan Liu[1,2,3,a] (iD)

AFFILIATIONS

[1] Collaborative Innovation Center of Chemistry for Energy Material, Shanghai Key Laboratory of Molecular Catalysis and Innovative Materials, Key Laboratory of Computational Physical Science, Department of Chemistry, Fudan University, Shanghai 200433, China
[2] Shanghai Qi Zhi Institution, Shanghai 200030, China
[3] Key Laboratory of Synthetic and Self-Assembly Chemistry for Organic Functional Molecules, Shanghai Institute of Organic Chemistry, Chinese Academy of Sciences, Shanghai 200032, China

Note: This paper is part of the JCP Special Topic on Chemical Design by Artificial Intelligence.
a)Author to whom correspondence should be addressed: zpliu@fudan.edu.cn

ABSTRACT

The surface of a material often undergoes dramatic structure evolution under a chemical environment, which, in turn, helps determine the different properties of the material. Here, we develop a general-purpose method for the automated search of optimal surface phases (ASOPs) in the grand canonical ensemble, which is facilitated by the stochastic surface walking (SSW) global optimization based on global neural network (G-NN) potential. The ASOP simulation starts by enumerating a series of composition grids, then utilizes SSW-NN to explore the configuration and composition spaces of surface phases, and relies on the Monte Carlo scheme to focus on energetically favorable compositions. The method is applied to silver surface oxide formation under the catalytic ethene epoxidation conditions. The known phases of surface oxides on Ag(111) are reproduced, and new phases on Ag(100) are revealed, which exhibit novel structure features that could be critical for understanding ethene epoxidation. Our results demonstrate that the ASOP method provides an automated and efficient way for probing complex surface structures that are beneficial for designing new functional materials under working conditions.

Published under an exclusive license by AIP Publishing. https://doi.org/10.1063/5.0084545

I. INTRODUCTION

The functionality of a solid material is much related to its surfaces that are exposed to complex environment.[1,2] It is notoriously challenging to characterize the surface than the bulk due to the added freedoms of atoms/molecules in diffusing, exchanging, and reacting with environment. In order to distinguish surface atoms, the surface probing techniques should ideally be capable of operating under the working conditions and achieve a high spatial–temporal resolution. Few experimental techniques, however, meet the high standard, and consequently, many surface-specific phenomena are hard to resolve to date, e.g., those under the high temperature and high pressure conditions for catalysis[3-5] and in the electric field and the surrounding of electrolytes for electrochemistry.[6-8]

New techniques are highly desirable in predicting the structure and functionalities of surfaces under working conditions.

With the advent of first-principles calculations, theoretical approaches have become an alternative tool in revealing the thermodynamics and kinetics of a surface in the past two decades.[9-16] The surface evolution under working conditions can be broadly considered as a phase change in the grand canonical (GC) ensemble where the chemical potential of species is pinned by environment. In the GC ensemble, the chemical composition and, thus, the number of atoms (N) in the simulation system are variable, which disallows the direct use of common simulation methods, e.g., molecular dynamics (MD) based on first-principles density functional theory (DFT) calculations. Instead, the trajectory for surface structure evolution can be retrieved by using the Monte Carlo method at the constant

chemical potential to mimic the system in the GC Monte Carlo (GCMC) simulation.[17,18] The continuous variation of the atomic number N in the system is therein approximated by a series of discrete frames changing with time t, each with fixed N(t). For example, Wexler *et al.*[17] using the GCMC method revealed the possible growing mechanism of silver surface oxide on the Ag(111) surface within a particular p(4 × 4) surface periodicity, where the structure candidate is generated randomly via the step-wise atom addition/removal followed by structure relaxation.

Despite the success in specific examples, two leading challenges in GCMC simulation hindered its wide applications, namely, (i) to accurately determine the chemical potential of species on the surface and (ii) to reveal the surface periodicity for the relevant, often the most stable, structure at given N. Obviously, both are related to the efficiency of potential energy surface (PES) exploration, which is required to compute the (configurational) entropy and to find the stable minima in different surface periodicities. Although many structure search methods are available to date, they do generally have their own problems, e.g., MD simulation is not efficient for corrugated PES due to the low ability in surmounting barriers; the common global optimization methods, such as genetic algorithm (GA)[19–21] and particle swarm optimization (PSO),[9,22] are generally too expensive in computation to apply for large surface systems and also do not follow reaction kinetics in evolving structures. For these reasons, the *ab initio* thermodynamics method has been more popularly utilized to construct the thermodynamics diagram for solid–gas interfaces.[11,16,23,24] The linkage between the total energy E at constant N and the Gibbs free energy G is established by using standard thermodynamics equations with appropriate approximations. The method only focuses on a limited number of surface compositions that are often manually generated in the predefined periodicity and also neglects the kinetics of structure evolution.

On the other hand, recent advances in machine-learning simulation[25–30] have provided new hope for fast and accurate PES evaluation. In particular, in a large material system, the PES computation speed using machine learning potential can be several orders of magnitude (>10^4) faster than DFT.[31,32] By integrating with stochastic surface walking (SSW) global optimization,[33–35] our group has shown in recent years that the thus-generated global neural network (G-NN) potential can be utilized for unbiased global structure search starting from a random initial guess.[32,36,37] This offers the possibility for the SSW-NN method to solve a wide range of heterogeneous catalysis problems, ranging from surface structure reconstruction to catalytic reaction prediction.[38–41]

Herein, facilitated by SSW-NN technique, we develop a general-purpose algorithm for automatic search of optimal surface phases (ASOPs) in the GC ensemble. The ASOP aims at identifying stable surface phases pinned by the given chemical potential of species. It can efficiently scan the vast configuration and composition spaces to find the most stable phase and also yield a trajectory to the most stable phase that mimics the surface phase evolution pathway. We demonstrate the ASOP method in the famous silver surface oxide challenge, i.e., thin oxide layer grown on Ag(111) and Ag(100) surfaces. Not only the known surface oxide phases, e.g., c(4 × 8) pattern on Ag(111), are reproduced, but also a zoo of low energy new surface phases are identified, which provides important

clues for understanding the surface oxide formation and the high ethene epoxidation activity of Ag(100) surface oxides.

II. ALGORITHM OF ASOP

Let we first recall the GCMC approach. We define the free energy of a surface system as $G(N, C_1, \ldots, C_k)$ with k species, and the chemical potential of species i (μ_i) is given by

$$\mu_i = \frac{\partial G}{\partial N_i}, \quad (1)$$

where N is the number of moving atoms on the surface and C_i is the concentration for species i on the surface with $C_i = N_i/N$. In the GC ensemble, all μ_i reach the equilibrium with the chemical potential of environment (μ_{ext}) to make $\mu_i - \mu_{i,ext} = 0$, and thus, in simulation, one needs to minimize the following difference:

$$\min(\mu_i - \mu_{i,ext}), \quad (2)$$

which can be achieved via the Metropolis MC algorithm to make the state selection according to the probability

$$p = \begin{cases} 1 & if \ \mu_i \le \mu_{i,ext}, \\ \exp\left[-\frac{\mu_i - \mu_{i,ext}}{kT}\right] & if \ \mu_i > \mu_{i,ext}, \end{cases} \quad (3)$$

as implemented in the GCMC algorithm. By continuously adding/removing atoms of species i, simulation can gradually reach the equilibrium state, where $\mu_i = \mu_{i,ext}$.

The GCMC simulation is a slow, sequential algorithm in nature. The structure operation, i.e., atom-wise addition/removal, generally neglects the surface periodicity that is, in fact, very important in real applications. With the increase of system size that explodes the possible composition space, the GCMC simulation based on DFT calculations becomes impractical.

In this work, we have designed a new algorithm for GC simulation with the following four features, aiming to more efficiently explore the configuration and composition spaces.

(i) An automated multi-grid algorithm is utilized to explore the composition space in different surface periodicities.
(ii) An automated initial structure generation is designed to yield structures at a valid periodicity.
(iii) The SSW global structure search based on G-NN potential is utilized to search for the configuration space in a given composition and periodicity.
(iv) A new MC scheme is designed to select a group of optimal phases based on the knowledge from the history of structure search.

The ASOP algorithm is parallel in nature since the composition space is discretized into an ensemble constituted by the elements in a series of grids from coarse to fine grids. The structure search is always parallelly performed, starting from the coarsest grid that can be simulated in small surface periodicity and then propagating toward the finer grids where the MC algorithm is utilized to screen out the energy favorable compositions by mapping grid elements from the coarse to fine grid. With the above improvements,

the ASOP can be utilized for the unbiased and automated search of optimal surface phases with simple input knowledge, i.e., the bulk crystal structure, the surface Miller index, and the chemical potential for species.

We emphasize that by using the SSW-NN global optimization for structure search, the ASOP method is not sensitive to the input guessed structure, i.e., no input structure dependence, and also greatly improves the efficiency of PES evaluation. The multi-grid method utilized in ASOP further eliminates the problems in exploring different surface periodicity that are commonly encountered in GCMC simulation.

Specifically, the ASOP algorithm constitutes three steps, and the flowchart is schematically shown in Fig. 1.

Step 1: Generating a series of grids, from coarse to fine grids, for the composition space. Each grid is associated with a unique supercell size with a particular periodicity, defined by the lattice parameters ($Latt_j$, where j is the index for grid) and the maximum number of atoms at the full layer (N_j), and an element in grid corresponds to a composition $C_m = \{C_1, \ldots, C_k\}$ (m is the index of the element in the grid). Thus, the phase vector (N_j, $Latt_j$, and C_m) is utilized as the unique entry of a phase registered in the phase database. Initially, we start from the coarsest grid (the smallest supercell), and all compositions are allowed to search with the equal probability of $p(C_m) = 1$. A number of compositions in the current grid are thus selected randomly as the phase candidates for step 2. The number of cycles in searching a grid (n_{cycle}) is set as zero.

Step 2: Using the SSW-NN method to search for the structure of phase candidates one-by-one. The SSW-NN search is performed with only a limited number of steps, generally below 300 steps. The current best structure for each phase and

their thermodynamic stability obtained from SSW-NN are stored and updated into the phase database. Now, the program increments n_{cycle} by 1 and moves to step 3.

Step 3: Using a MC algorithm to update the phase probability $p(C_m)$ for the next grid. The next grid can still be the same as the current grid if n_{cycle} is below a preset value ($n_{maxcycle}$) or is a new grid generated from step 1 when $n_{maxcycle}$ is reached. Now, the next grid becomes the current grid and goes back to step 2.

As shown in Fig. 1, the ASOP simulation will scan the PES from the coarse grid in the small supercell to the fine grid in the large supercell. The free energy of the phases in the database will thus be determined, as illustrated by the filled color in each grid. In the end, the ASOP simulation can provide the most stable phases (e.g., the deep blue color for the grid element in Fig. 1) and also produce a low energy channel for the phase evolution with the change of composition.

In the following, we give a detailed account on the algorithm for the three steps.

A. Step 1: Generation of composition grids

This step enumerates all the possible supercells, based on which a composition grid is generated for each supercell. The primitive cell p(1×1) for a given (hkl) surface, defined by a [$\mathbf{u}$, $\mathbf{v}$] vector, can be cleaved from the bulk crystal. Any supercells of the surface defined by [$\mathbf{u}'$, $\mathbf{v}'$] vector can then be obtained by using the following equations:

$$\begin{pmatrix} \mathbf{u}' \\ \mathbf{v}' \end{pmatrix}_{newslab} = TM \times \begin{pmatrix} \mathbf{u} \\ \mathbf{v} \end{pmatrix}_{primslab}, \qquad (4)$$

$$A = |TM| = \begin{vmatrix} a_1 & b_1 \\ a_2 & b_2 \end{vmatrix}, \qquad (5)$$

where the transition matrix (TM) must be positive definite (determinant $A > 0$) and its matrix element can be enumerated, e.g., from -10 to 10 in this work. The A value from Eq. (5) is a scaled area, being the multiple of the primitive cell size. Based on the Niggli reduced cell theory,[42] only the supercell with the angle between $\mathbf{u}'$ and $\mathbf{v}'$ is in between $60°$–$90°$ and $|\mathbf{u}'| \geq |\mathbf{v}'|$ are kept as the valid/non-redundant supercell candidate. To further reduce the computational cost, we also limit the maximum of lattice ratio ($|\mathbf{u}'|/|\mathbf{v}'|$) to be less than 3, which removes too narrow supercells, known to be uncommon from surface science studies.

Next, we can define a composition grid for each supercell with each grid element corresponding to a composition (see Fig. 2). The grid with the smallest A (scaled area) is thus the coarsest grid, and the finer the grid, the larger the A value is. All the grids will be sorted by their A value and labeled in the phase database.

Figure 2 uses the surface oxide AgO_x grown on the Ag(111) surface to illustrate the composition grid generation. By enumeration, we can obtain TM (2, 0; -1, 2) and generate a ($2 \times \sqrt{3}$) periodicity of the Ag(111) supercell, where A is 4. By limiting the maximum Ag and O coverage to 1 ML (a preset parameter) in this work, we can thus get the composition grid of (4×4) to represent the Ag:O composition variation from $N_{Ag}:N_O = 4:1$ to $N_{Ag}:N_O = 1:4$; see Fig. 2, top
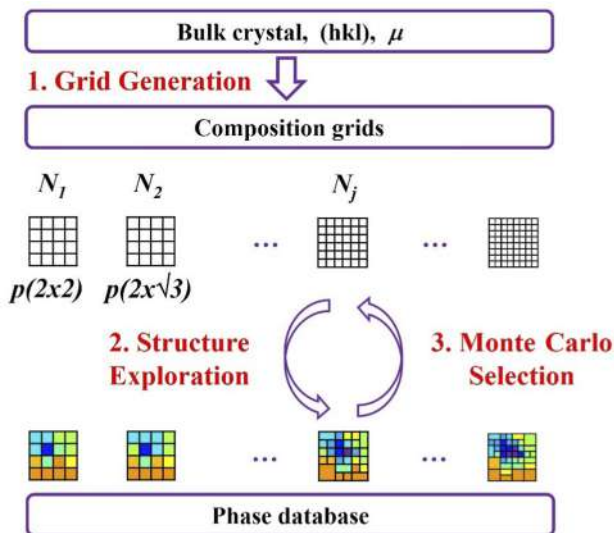

FIG. 1. Flowchart of the ASOP algorithm that contains three steps. Simulation starts from simple inputs, i.e., bulk crystal structure, the surface index, and the chemical potential of species, and produces the phase stability at different compositions, as the colored grids shown here.
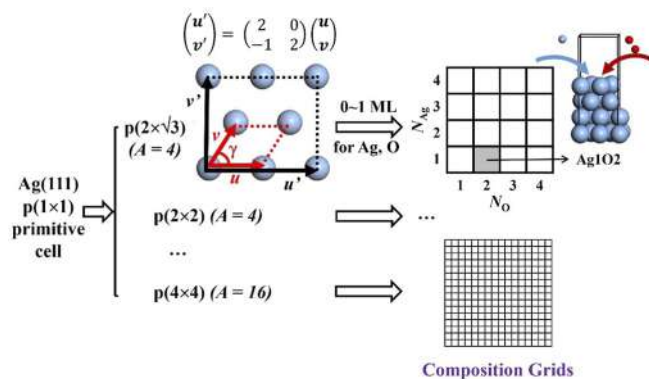
FIG. 2. Composition grid generation illustrated with Ag(111). The procedure for generating the grid of $(2 \times \sqrt{3})$ reconstructed Ag(111) is shown in detail on the top panel. Each element in the grid represents a composition, as shown in the shaded area, i.e., Ag_1O_2 [one Ag atom and two O atoms on the $(2 \times \sqrt{3})$ reconstructed Ag(111) slab; see the inset].

grid. The entry for the Ag_1O_2 phase with $(2 \times \sqrt{3})$ Ag(111) periodicity, for example, in the phase database can be registered using the grid label for $(2 \times \sqrt{3})$ and the grid element, $N_{Ag} = 1$ and $N_O = 2$.

B. Step 2: Structure exploration for compositions in a grid

This step aims at identifying the favorable compositions by scanning selected grid elements in the current grid. The central task is to find the optimal structure for each grid element. Since the initial structure for a given composition is generally unknown, an unbiased global minimum (GM) search is invoked by using SSW-NN global

optimization implemented in the LASP (Large-scale Atomic Simulation with neural network Potential) code (The details of the SSW-NN method can be found in the supplementary material). Step 2 is the central part of the ASOP algorithm, which further contains four stages, as illustrated in Fig. 3. These four stages are executed repeatedly until all the target grid elements have been explored. Because the structure search for each grid element is independent, the algorithm can run efficiently in parallel.

Stage A: Initial structure generation. For a given composition in a grid, if the initial structure is not available, we generate the initial structure by adding atoms one-by-one into the surface slab. Every newly arrived atom is randomly added but needs to be not too close (<1.5 Å) to or too far away (>3 Å) from the other surface atoms. Once the atom is added, a local structure relaxation based on G-NN potential is performed. The atom addition is repeated until the given composition is reached. On the other hand, if the target composition in the grid has been searched previously, the best structure in the previous run will be inherited as the initial structure.

Stage B: SSW global structure search. Starting from an initial structure, SSW global optimization with a limited number of steps (typically <400 steps) is performed to find a current best structure. For each single SSW-NN run, it is not important whether the current best structure is the GM since the energy favorable compositions will be repeatedly searched, particularly, in the finer grids.

Stage C: Self-learning of G-NN potential. From the SSW-NN structure search trajectory, we will select a number of structures for benchmarking G-NN PES against the DFT PES. If the stability order of the phases from G-NN result is different from that from the DFT, retraining of G-NN potential
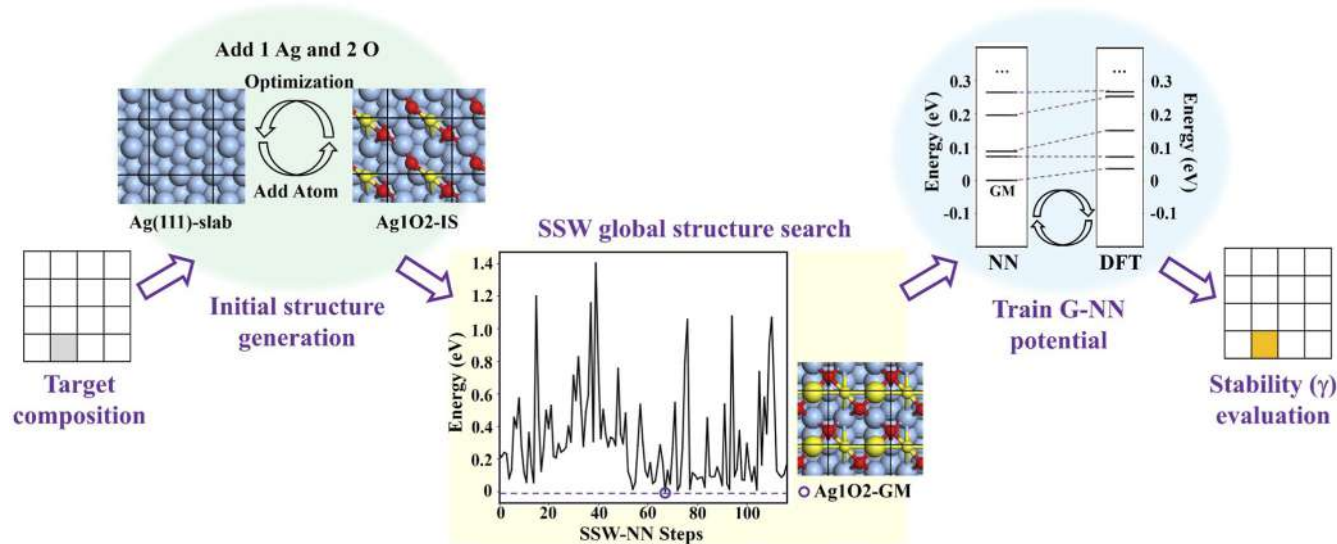

FIG. 3. Structure exploration illustrated by searching the structure of Ag_1O_2 composition on $(2 \times \sqrt{3})$-Ag(111). There are four stages: initial structure generation, SSW-NN global structure search, G-NN potential retraining, and thermodynamics stability evaluation.

is performed by adding these phases into database. This step is essential, particularly at the initial stages, which can greatly improve the reliability of G-NN PES.

Stage D: Thermodynamics stability evaluation. With the current best structure obtained from SSW-NN, its stability, the surface free energy, can be evaluated using

$$\gamma = \frac{G_{X/surf} - G_{surf} - \sum_{i=1}^{k} N_i \mu_{i,ext}}{A},\qquad(6)$$

where $G_{X/surf}$, G_{surf} are the free energy of the surface with all incoming species (i from 1 to k) and the clean surface, respectively, N_i is the number of atoms for the i species on the surface, $\mu_{i,ext}$ is the chemical potential of the i species defined by environment, and A is the scaled area given by Eq. (5). In searching for phases with the lowest possible γ, the thermodynamics equilibrium can be finally established that minimizes $(\mu_i - \mu_{i,ext})$.

Figure 3 illustrates the above four stages exampled by the Ag_1O_2 composition grown on Ag(111) in a grid of the $(2 \times \sqrt{3})$ supercell. Starting from the randomly generated initial structure, SSW-NN can help to locate a local best structure in less than 100 SSW steps and the low energy structure from the SSW trajectories is utilized to improve the accuracy of G-NN PES by benchmarking with DFT calculations. Finally, the stability of the composition at the grid is computed and recorded in the phase database.

C. Step 3: Favorable composition determination by Monte Carlo selection

Once the stability γ of all target compositions is updated in the phase database, we are in a position to rank the favorable compositions and select the compositions for the next cycle of structure exploration. The composition favorableness for a grid element at C_m can be measured by its probability $p(C_m)$ weighted over all grid elements ($g = 1\ldots Ng$, where Ng is the total number of grid points) using Eq. (7), where ε_m is the energy at the grid C_m and ε_0 is the lowest value of ε_m in the grid [Eq. (8)]. ε_m is defined as the lowest value over $\varepsilon_{m,n}$ [Eq. (8)], where n runs over the lowest energy phases in the phase database that are collected in history. Each $\varepsilon_{M,n}$ can be evaluated using the function in Eq. (9), being a Gaussian-smeared γ_n by measuring the composition distance $\|\mathbf{q}_m - \mathbf{q}_n\|$ between composition C_m and composition C_n, where $\mathbf{q}$ is the fractional coordinate vector of a composition in the grid [e.g., Ag_2O_1 in the $(2 \times \sqrt{3})$ cell, $\mathbf{q} = (2/4, 1/4)$]. In Eqs. (7)–(9), we typically set the smearing parameter as $\sigma = 0.1$ and the Boltzmann-type weighting variable as $\beta = 0.5$–1.5 depending on n_{cycle} ($\beta = 0.5 \times n_{cycle}$). The smaller β value facilitates the sampling of the higher energy composition,

$$p(C_m) = \frac{\exp(\beta(\varepsilon_m - \varepsilon_0)/\varepsilon_0)}{\sum_{k=1}^{Ng} \exp(\beta(\varepsilon_k - \varepsilon_0)/\varepsilon_0)},\qquad(7)$$

$$\varepsilon_m = \min(\varepsilon_{m,n}), \ \varepsilon_0 = \min(\varepsilon_m),\qquad(8)$$

$$\varepsilon_{m,n} = \gamma_n \exp\left(-\frac{\|\mathbf{q}_m - \mathbf{q}_n\|^2}{2\sigma^2}\right).\qquad(9)$$

If n_{cycle} is smaller than $n_{maxcycle}$ (3 in this work), we will continue the structure search at the same grid. If n_{cycle} equals $n_{maxcycle}$, we will move onto the next unexplored grid. By going over all the composition in the grid one-by-one using the MC algorithm, we will screen out the compositions for the further structure search: a composition C_m is selected if the randomly generated number in between (0, 1) is smaller than its $p(C_m)_f$. If the number of compositions survived from MC is too many, we use a hard limit (=15) to restrict the search for the top $p(C_m)$ compositions. Now, the ASOP simulation goes back to step 2 for a new cycle.

While the ASOP simulation enumerates all possible periodicities by scanning all supercell grids, it can actually be finished with low cost. Apart from the utilization of machine-learning potential in all simulations, it relies on the multi-grid algorithm to reduce the computational cost, where the composition zone with poor energetics can be labeled at the early stages (in small supercell calculations) and less explored at the later stages (in large supercell calculations). In the meantime, the MC scheme allows the poor energetic phase being selected with a finite probability, which helps to identify the stable phase with a sharp composition window.

III. APPLICATIONS TO AgOx SURFACE OXIDES

We have applied the ASOP method to determine the silver oxide structures on Ag(111) and Ag(100). This system is of great interest due to the wide industrial application of the Ag catalyst for ethene epoxidation. While the surface oxides grown on Ag(111) have been well documented, few studies have been carried out for Ag(100) due to the lack of experimental data, although Ag(100) was shown to be a better facet for epoxidation.[43] A major task in this field is to identify the stable structure of surface oxides grown on different Ag surfaces under the experimental conditions, e.g., 500 K and 1 atm O2 pressure.[39,44–46]

A. Surface oxides on Ag(111)

In searching for surface oxides on Ag(111), we set the range of grid dimension from 4 to 16, i.e., Ag_xO_y with x and y from 1–4 to 1–16, which generates 52 distinct grids (supercells) and 6924 compositions in total. For each grid, a maximum of 15 compositions can be selected and three cycles ($n_{maxcycle} = 3$) of SSW-NN structure search are performed. Among 6924 possible compositions, the ASOP simulation explicitly explores 1444 distinct compositions and visits 388 331 minima by SSW-NN in total. The whole simulation finished in 120 h on a Xeon(R) Gold 6126 CPU (2.60 GHz, 80 CPU Cores). Considering that the SSW-NN method in structural exploration is about 10^4 times faster than DFT, the same work would take 5000 years using DFT calculations.

The G-NN potential utilized is the Ag–C–H–O quaternary potential developed for the LASP project and released in the website (www.lasphub.com). In the ASOP simulation, this G-NN potential is benchmarked with DFT calculations and further improved to describe the surface oxides (see also the supplementary material). The final G-NN potential learns totally 50 131 structures in the dataset, with the root mean square (rms) errors for the energy and force to be 2.76 meV/atom and 0.08 eV/Å, respectively. Chemical potentials μ_{Ag} and μ_O are set to be the enthalpy of bulk Ag per atom and half of μ_{O2}, respectively. μ_{O2} is computed by using the
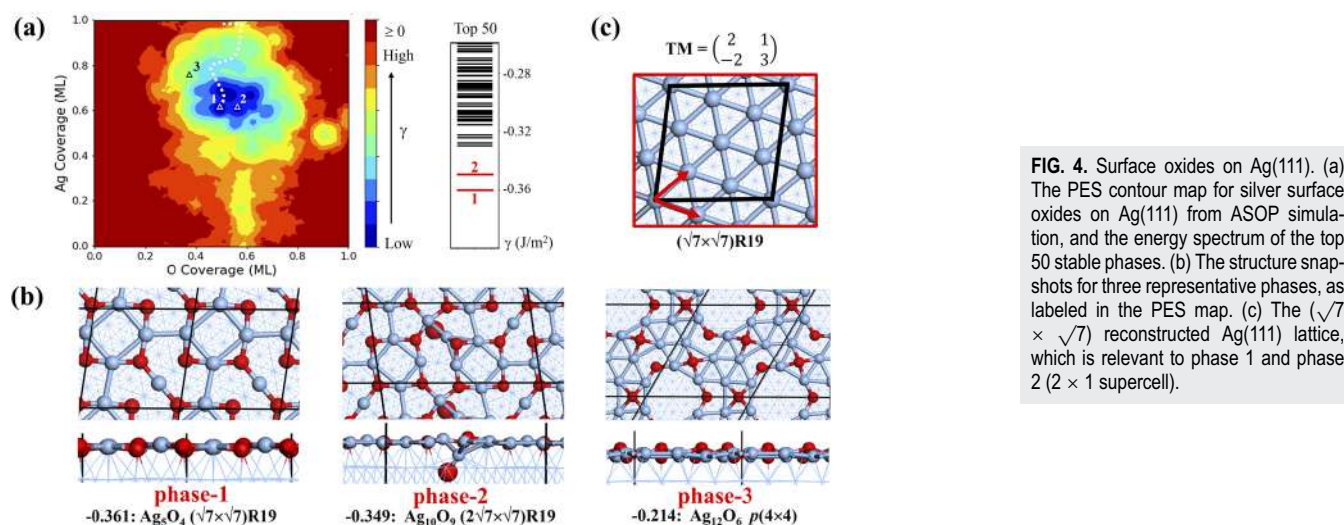
FIG. 4. Surface oxides on Ag(111). (a) The PES contour map for silver surface oxides on Ag(111) from ASOP simulation, and the energy spectrum of the top 50 stable phases. (b) The structure snapshots for three representative phases, as labeled in the PES map. (c) The ($\sqrt{7} \times \sqrt{7}$) reconstructed Ag(111) lattice, which is relevant to phase 1 and phase 2 (2 × 1 supercell).

standard molar enthalpy of the formation of Ag_2O[10] with respect to the Ag metal corrected by the free energy contribution of gas phase O_2 at the typical catalytic ethene epoxidation condition (500 K, 1 bar)[47] (see also the supplementary material).

Figure 4(a) summarizes the results for Ag(111) after the ASOP simulation. The PES contour map (we have shown the details for plotting the map in the supplementary material) in Fig. 4(a) plots the relative stability at different Ag:O compositions collected from the database (each composition may correspond to a different supercell). Obviously, the zone of stable surface oxides ($\gamma < 0$) is in a wide window for the O coverage about 0.3–0.8 ML, while the most stable zone [blue zone in Fig. 4(a)] occurs at the Ag coverage of about 0.5–0.8 ML and the O coverage of about 0.4–0.7 ML. The right-hand energy spectrum more clearly shows the energy sequence for the

most stable surface oxides, where the lowest γ is −0.361 J/m², and there are many phases with the γ value around −0.3 J/m².

We then examined the structure of the stable phases, and three representative phases are shown in Fig. 4(b) and Table I, namely, phase 1, phase 2, and phase 3 corresponding to 1, 2, and 3 labeled in the PES map, respectively. The geometries of selected surface oxides (e.g., those having deep oxidation) are shown in Table S4 of the supplementary material.

Phase 1, the most stable phase from ASOP, has the O and Ag coverage of 0.50 and 0.62 ML (Ag_5O_4), respectively. It is exactly the well-known c(4 × 8) structure on Ag(111) first revealed in the experiment[48] and confirmed later by *ab initio* thermodynamics,[16,30] which has the cross-linked [AgO$_4$] and [Ag$_4$O$_4$] motifs sharing with four-fold O atoms. Due to the high O concentration (Ag_5O_4), this

TABLE I. The stoichiometry, surface periodicity, Ag and O coverage (C), and surface free energy γ for some representative silver surface oxides found in this work that are compared, if available, to literature studies [in both experiments (expt.) and DFT calculations].

Supporter	Stoichiometry	Periodicity	C(Ag) (ML)	C(O) (ML)	γ (J/m²)	Literature (expt./DFT)
	(phase 1) Ag_5O_4	($\sqrt{7} \times \sqrt{7}$)R19	0.62	0.50	−0.361 (−0.181/−0.160)[a]	Reference 48/16
	(phase 2) $Ag_{10}O_9$	($2\sqrt{7} \times \sqrt{7}$)R19	0.62	0.56	−0.349	· · ·
	(phase 3) $Ag_{12}O_6$	p(4 × 4)	0.75	0.38	−0.214 (−0.108/−0.118)[a]	References 51 and 52/16
Ag(111)	$Ag_{32}O_{15}$	p(4 × 5$\sqrt{3}$)	0.80	0.38	−0.201 (−0.100/−0.099)[a,b]	Reference 52/16
	$Ag_{24}O_{12}$	c(3 × 5$\sqrt{3}$)	0.80	0.40	−0.202 (−0.078/−0.093)[a,b]	Reference 52/16
	$Ag_{27}O_{18}$	p(7 × 7)	0.55	0.37	−0.129 (−0.114/−0.120)[a,b]	References 16 and 46/16
	$Ag_{14}O_{36}$	p(7 × 7)	0.29	0.73	−0.098 (−0.029/−0.002)[a,b]	References 16 and 46/16
	(phase 1) Ag_7O_5	($2\sqrt{2} \times 2\sqrt{2}$)R45	0.88	0.62	−0.364	· · ·
	(phase 2) Ag_3O_2	($2\sqrt{2} \times \sqrt{2}$)R45	0.75	0.50	−0.339	Reference 53/23
Ag(100)	Ag_4O_2	c(2 × 2)	1	0.50	−0.238	Reference 53/23
	Ag_0O_8	c(4 × 6)	0	0.33	−0.258[b]	Reference 54/23
	Ag_0O_1	p(2 × 2)	0	0.25	−0.220	Reference 54/23

[a]The data in the bracket are the values calculated without vdW correction (D3) in this work (left) and the value from Ref. 16 (right).
[b]These structures are not in the ASOP simulation results due to the large surface periodicity and are calculated independently.

structure was postulated to be the critical transition phase toward those with subsurface O and further to Ag_2O films.[16,49]

Phase 2 is the second lowest phase with the O and Ag coverage at 0.56 and 0.62 ML, respectively ($Ag_{10}O_9$), which has not been reported in the experiment. The structure can be regarded as the (2 × 1) supercell of phase 1 with an extra O atom addition (red big ball in Fig. 5) into the subsurface and, as a result, a Ag atom being slightly squeezed out from the surface plane. Indeed, the subsurface oxygen has been observed in the surface science experiment, mimicking the catalytic condition,[49] and our results confirm that the cost to have the subsurface O is only 0.012 J/m^2 increase in γ.

Phase 3 has the O and Ag coverage of 0.38 and 0.75 ML, respectively ($Ag_{12}O_6$), which is 0.147 J/m^2 above phase 1. The structure corresponds to the commonly observed "p(4 × 4)" phase in surface science studies for Ag(111) under low O_2 pressures (<1 Torr).[50–52] The most obvious characteristic is the presence of the Ag(111)-like metallic Ag_6 motif. From the PES map, this phase is, in fact, not the most stable phase under high O_2 pressures (1 bar).

B. Surface oxides on Ag(100)

Encouraged by the success in (111), we have searched the surface oxides on Ag(100) with the input changing from (111) to (100). Most of the settings in the ASOP simulation is identical to those for Ag(111), except that the range of the grid dimension is limited to be 4–12. The final composition space of Ag(100) contains 44 distinct grids (supercells) and 3775 compositions in total. Among them, the ASOP simulation explicitly explores 1417 distinct compositions, which in total visits 329 981 minima by SSW-NN. The whole simulation finished in 90 hours on a Xeon(R) Gold 6126 CPU (2.60 GHz, 80 CPU Cores).
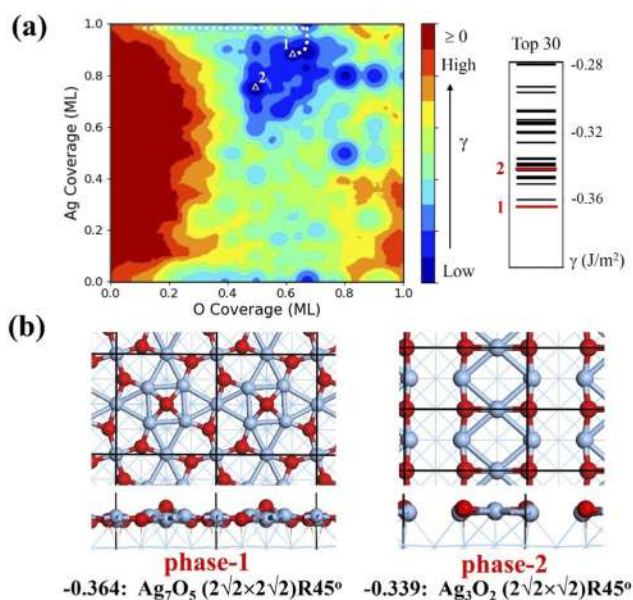

FIG. 5. Surface oxides on Ag(100). (a) The PES contour map for silver surface oxides on Ag(100) from ASOP simulation and the energy spectrum of the top 30 stable phases. (b) The structure snapshots for two representative phases, as labeled in the PES map.

The results for Ag(100) are summarized in Fig. 5(a). Compared to Ag(111), the surface oxide zone ($\gamma < 0$) of Ag(100) in the PES map of Ag(100) appears to be not localized near a particular composition but spreads out in a wide region for the O coverage of above 0.3 ML. This is consistent with the lower Ag coordination of (100) that can better accommodate O atoms. The energy favorable surface oxides occur at the region with the Ag and O coverage being 0.6–1.0 and 0.5–0.9 ML, respectively. As shown in the energy spectrum, these low energy surface oxides generally are close in energetics, γ being −0.30 to −0.36 J/m^2, and the most stable one has γ of −0.364 J/m^2. This suggests that the PES of surface oxides on Ag(100) is glassy with many possible configurations under catalytic conditions. We select two representative structures, phase 1 and phase 2 shown in Fig. 5(b) (also indicated in the PES map) and Table I, to illustrate the structures on Ag(100). The geometries of selected surface oxides (e.g., those having deep oxidation) are shown in Table S4 of the supplementary material.

Phase 1 is the most stable phase identified, which has a Ag_7O_5 stoichiometry in the ($2\sqrt{2} \times 2\sqrt{2}$)R45° supercell with the O and Ag coverage being 0.62 and 0.88 ML, respectively. The Ag_7O_5 phase on Ag(100) contains the [Ag_4O] motif and the planar coordinated [AgO_4] motif. Compared to the most stable c(4 × 8) phase on Ag(111), the Ag_7O_5 phase on Ag(100) possesses higher surface atomic density with three major distinctions: (i) it has a four-coordinated O on the surface, which is not present in the c(4 × 8) phase on (111); (ii) it has one additional Ag atom as the linkage; and (iii) all the four Ag–O in the [AgO_4] motif pattern are equally bonded. It is also noted that, while the O coverage is higher on the Ag_7O_5 phase than that in the c(4 × 8) phase, all the oxygen atoms are located on the surface: no subsurface O is present. This makes the Ag(100) surface to have the higher ability to store O atoms.

Phase 2 has a Ag_3O_2 stoichiometry in the ($2\sqrt{2} \times \sqrt{2}$)R45° supercell, with the O and Ag coverage being 0.50 and 0.75 ML, respectively. It is only 0.025 J/m^2 less stable than phase 1. This structure has been reported previously in the experiment as a missing-row reconstruction pattern since 25% Ag atoms of the top Ag(100) layer are missing upon the addition of O atoms.[23,53,54] Similar to the p(4 × 4) phase on Ag(111), this structure maintains the characteristics of Ag metal sites and thus can be considered as the consequence of partial oxidation.

We would like to mention that the PES contour map can also provide important knowledge on the low energy channel for the phase evolution. By following low energy compositions, we can readily identify a path connecting the bare Ag surface to the most stable phase, as the white dashed lines in Fig. 4(a) for Ag(111) and Fig. 5(a) for Ag(100). In both paths, the oxygen atoms first populate onto the Ag surface that reaches a saturated coverage when the surface Ag atoms remain constant. Next, in order to further decrease the free energy, surface Ag atoms start to migrate away (into bulk) accompanied by the reduction of the surface O atom coverage, which leads to the formation of surface oxides (blue zone in Figs. 4(a) and 5(a)) and finally achieves the thermodynamic equilibrium. From our PES maps, the low-oxygen-pressure surface phases as observed in surface science studies may well not be the intermediate, leading to the most stable phase under the high O_2 pressure conditions of ethene epoxidation,

since they are deviated from the low energy channel (see phase 3 in Fig. 4 and phase 2 in Fig. 5).

IV. CONCLUSION

To recap, this work develops a machine-learning based ASOP method to search for optimal surface phases in the grand canonical ensemble. This method can effectively explore the surface phase space with different compositions and surface periodicities. The key features of the ASOP method include a multi-grid algorithm to explore the composition space, the SSW-NN global optimization for fast structure exploration, and the Monte Carlo scheme to screen out the favorable compositions. For the great power of SSW-NN in finding the global minima of complex systems, the ASOP method is expected to be generally applicable to surface systems, e.g., having structural defects (vacancies) and supporting clusters.

The ASOP method is demonstrated in exploring the silver surface oxides grown on both Ag(111) and Ag(100) under the catalytic relevant conditions. The previously known phases on Ag(111) are successfully identified, and new surface oxide phases on Ag(100) are revealed. Our results show that unlike Ag(111), the surface oxides on Ag(100) have a glassy PES with many energetically close structures, where new Ag–O patterns emerge. The presence of ethene may, thus, further alter the most stable surface phase in Ag(100) under the reaction conditions. The current knowledge can be of key value for understanding silver oxidation behaviors during ethene epoxidation.

SUPPLEMENTARY MATERIAL

See the supplementary material for the details of methodology on the architecture of global neural network potential, SSW-NN simulation, DFT calculations, the Gibbs free energy computation, the benchmark of G-NN potential against DFT, the PES contour map construction, the geometries of surface oxides with the increasing of O coverage, and XYZ coordinates for the stable silver surface oxides shown in Figs. 4(b) and 5(b).

ACKNOWLEDGMENTS

AUTHOR DECLARATIONS

Conflict of Interest

The authors have no conflicts to disclose.

DATA AVAILABILITY

The data that support the findings of this study are available from the corresponding author upon reasonable request.

REFERENCES

[1] H. Wang, L. Zhang, Z. Chen, J. Hu, S. Li, Z. Wang, J. Liu, and X. Wang, Chem. Soc. Rev. **43**, 5234 (2014).

[2] H. Over, Y. D. Kim, A. P. Seitsonen, S. Wendt, E. Lundgren, M. Schmid, P. Varga, A. Morgante, and G. Ertl, Science **287**, 1474 (2000).

[3] F. F. Tao and M. Salmeron, Science **331**, 171 (2011).

[4] L. Nguyen, F. F. Tao, Y. Tang, J. Dou, and X.-J. Bao, Chem. Rev. **119**, 6822 (2019).

[5] F. F. Tao and P. A. Crozier, Chem. Rev. **116**, 3487 (2016).

[6] H. A. Hansen, J. Rossmeisl, and J. K. Nørskov, Phys. Chem. Chem. Phys. **10**, 3722 (2008).

[7] Y.-H. Fang and Z.-P. Liu, ACS Catal. **4**, 4364 (2014).

[8] Y.-H. Fang and Z.-P. Liu, J. Phys. Chem. C **114**, 4057 (2010).

[9] R. J. Bunting, X. Cheng, J. Thompson, and P. Hu, ACS Catal. **9**, 10317 (2019).

[10] W.-X. Li, C. Stampfl, and M. Scheffler, Phys. Rev. Lett. **90**, 256102 (2003).

[11] J. Rogal, K. Reuter, and M. Scheffler, Phys. Rev. Lett. **98**, 046101 (2007).

[12] N. D. McClenaghan, P. Hu, and C. Hardacre, Surf. Sci. **464**, 223 (2000).

[13] S. Piccinin, C. Stampfl, and M. Scheffler, Surf. Sci. **603**, 1467 (2009).

[14] A. Michaelides, K. Reuter, and M. Scheffler, J. Vac. Sci. Technol. A **23**, 1487 (2005).

[15] Z.-Y. Zhu, Y.-F. Li, C. Shang, and Z.-P. Liu, J. Phys. Chem. C **125**, 17088 (2021).

[16] N. M. Martin, S. Klacar, H. Grönbeck, J. Knudsen, J. Schnadt, S. Blomberg, J. Gustafson, and E. Lundgren, J. Phys. Chem. C **118**, 15324 (2014).

[17] R. B. Wexler, T. Qiu, and A. M. Rappe, J. Phys. Chem. C **123**, 2321 (2019).

[18] E. Tylianakis and G. E. Froudakis, J. Comput. Theor. Nanosci. **6**, 335 (2009).

[19] L. B. Vilhelmsen and B. Hammer, J. Chem. Phys. **141**, 044711 (2014).

[20] Q. Wang, A. R. Oganov, Q. Zhu, and X.-F. Zhou, Phys. Rev. Lett. **113**, 266101 (2014).

[21] M. Sierka, T. K. Todorova, J. Sauer, S. Kaya, D. Stacchiola, J. Weissenrieder, S. Shaikhutdinov, and H.-J. Freund, J. Chem. Phys. **126**, 234710 (2007).

[22] S. Lu, Y. Wang, H. Liu, M.-s. Miao, and Y. Ma, Nat. Commun. **5**, 3666 (2014).

[23] A. Stierle, I. Costina, S. Kumaragurubaran, and H. Dosch, J. Phys. Chem. C **111**, 10998 (2007).

[24] T. E. Jones, T. C. R. Rocha, A. Knop-Gericke, C. Stampfl, R. Schlögl, and S. Piccinin, Phys. Chem. Chem. Phys. **17**, 9288 (2015).

[25] J. Behler, J. Chem. Phys. **145**, 170901 (2016).

[26] T. Mueller, A. Hernandez, and C. Wang, J. Chem. Phys. **152**, 050902 (2020).

[27] Q. Lin, Y. Zhang, B. Zhao, and B. Jiang, J. Chem. Phys. **152**, 154104 (2020).

[28] Y. Yang, O. A. Jiménez-Negrón, and J. R. Kitchin, J. Chem. Phys. **154**, 234704 (2021).

[29] M. S. Jørgensen, H. L. Mortensen, S. A. Meldgaard, E. L. Kolsbjerg, T. L. Jacobsen, K. H. Sorensen, and B. Hammer, J. Chem. Phys. **151**, 054111 (2019).

[30] H. L. Mortensen, S. A. Meldgaard, M. K. Bisbo, M.-P. Christiansen, and B. Hammer, Phys. Rev. B **102**, 075427 (2020).

[31] J. Behler, J. Phys.: Condens. Matter **26**, 183001 (2014).

[32] S.-D. Huang, C. Shang, P.-L. Kang, and Z.-P. Liu, Chem. Sci. **9**, 8644 (2018).

[33] C. Shang and Z.-P. Liu, J. Chem. Theory Comput. **9**, 1838 (2013).

[34] X.-J. Zhang, C. Shang, and Z.-P. Liu, J. Chem. Theory Comput. **9**, 3252 (2013).

[35] C. Shang, X.-J. Zhang, and Z.-P. Liu, Phys. Chem. Chem. Phys. **16**, 17845 (2014).

[36] S.-D. Huang, C. Shang, X.-J. Zhang, and Z.-P. Liu, Chem. Sci. **8**, 6327 (2017).

[37] S. Ma, C. Shang, and Z.-P. Liu, J. Chem. Phys. **151**, 050901 (2019).

[38] Q.-Y. Liu, C. Shang, and Z.-P. Liu, J. Am. Chem. Soc. **143**, 11109 (2021).

[39] D. Chen, P.-L. Kang, and Z.-P. Liu, ACS Catal. **11**, 8317 (2021).

[40] P.-L. Kang, C. Shang, and Z.-P. Liu, Acc. Chem. Res. **53**, 2119 (2020).

[41] S. Ma and Z.-P. Liu, ACS Catal. **10**, 13213 (2020).

[42] Y. Yang, C. Cai, J. Lin, L. Gong, and Q. Yang, Micron **96**, 9 (2017).

[43] P. Christopher and S. Linic, J. Am. Chem. Soc. **130**, 11264 (2008).

[44] T. Pu, H. Tian, M. E. Ford, S. Rangarajan, and I. E. Wachs, ACS Catal. **9**, 10727 (2019).

[45] S. Böcklein, S. Günther, and J. Wintterlin, Angew. Chem., Int. Ed. **52**, 5518 (2013).

[46] A. Reicho, A. Stierle, I. Costina, and H. Dosch, Surf. Sci. **601**, L19 (2007).

[47] R. D. Lide, *CRC Handbook of Chemistry and Physics*, 95th ed. (CRC Press, New York, 2015).

[48] J. Schnadt, J. Knudsen, X. L. Hu, A. Michaelides, R. T. Vang, K. Reuter, Z. Li, E. Laegsgaard, M. Scheffler, and F. Besenbacher, Phys. Rev. B **80**, 075424 (2009).

[49] J. Derouin, R. G. Farber, M. E. Turano, E. V. Iski, and D. R. Killelea, ACS Catal. **6**, 4640 (2016).

[50] G. Rovida, F. Pratesi, M. Maglietta, and E. Ferroni, Surf. Sci. **43**, 230 (1974).

[51] M. Schmid, A. Reicho, A. Stierle, I. Costina, J. Klikovits, P. Kostelnik, O. Dubay, G. Kresse, J. Gustafson, E. Lundgren, J. N. Andersen, H. Dosch, and P. Varga, Phys. Rev. Lett. **96**, 146102 (2006).

[52] J. Schnadt, A. Michaelides, J. Knudsen, R. T. Vang, K. Reuter, E. Lægsgaard, M. Scheffler, and F. Besenbacher, Phys. Rev. Lett. **96**, 146101 (2006).

[53] M. Rocca, L. Savio, L. Vattuone, U. Burghaus, V. Palomba, N. Novelli, F. B. de Mongeot, U. Valbusa, R. Gunnella, G. Comelli, A. Baraldi, S. Lizzit, and G. Paolucci, Phys. Rev. B **61**, 213 (2000).

[54] I. Costina, M. Schmid, H. Schiechl, M. Gajdoš, A. Stierle, S. Kumaragurubaran, J. Hafner, H. Dosch, and P. Varga, Surf. Sci. **600**, 617 (2006).